RESEARCH ARTICLE

An application of the localized weighted ensemble Kalman filter for ocean data assimilation

Yan Chen[1] ⬤ | Weimin Zhang[1,2] | Pinqiang Wang[1]

[1]College of Meteorology and Oceanology,
National University of Defense
Technology, Changsha, China

[2]Laboratory of Software Engineering for
Complex Systems, Changsha, China

Correspondence
W. Zhang, College of Meteorology and
Oceanology, National University of
Defense Technology, Changsha 410073,
China.
Email: wmzhang104@139.com

Funding information
National Key R&D Program of China,
Grant/Award Number: 2018YFC1406202;
National Natural Science Foundation of
China, Grant/Award Number: Grant No.
41675097

Abstract

We presented a new local particle filter named the localized weighted ensemble Kalman filter (LWEnKF), which was tested and verified using a simple high-dimensional Lorenz 96 model. A revised LWEnKF, the proposal weights calculation of which is modified through localization to prevent filter degeneracy for real geophysical models, is explored further in this article and shows lots of potential in the implementation of real complex models. For geophysical models, the ocean dynamics changes slowly compared with that of the atmosphere. With a relatively low resolution, it is weakly nonlinear in the surface layers of the ocean model used in this article, which fits the linear and Gaussian assumptions of the EnKF but could be a challenge for particle filters in the data assimilation process. With only 50 particles, the LWEnKF assimilates the sea-surface temperature (SST), sea-surface height (SSH), temperature, and salinity profiles with affordable computational cost, providing a reasonable forecast. Moreover, the LWEnKF is compared with the ensemble Kalman filter (EnKF) and the local particle filter (PF). For observed variables, the LWEnKF performs comparably to the EnKF, as the observation operator is linear. For unobserved variables, the LWEnKF provides more accurate forecasts than the EnKF, since the latter considers only the correlations, while the former considers higher-order moments. The local PF ensemble does not converge to the observed solution in an ample amount of time in this study, which needs further investigation.

KEYWORDS

ensemble Kalman filter, localization, ocean data assimilation, particle filter, proposal density

1 | INTRODUCTION

The ensemble Kalman filter (EnKF) and its derived algorithms have been applied widely and successfully in ocean data assimilation (DA), but its linear and Gaussian assumptions are not consistent with actual complex ocean models. Recently, the particle filter (PF) has been developed, substantially for application to nonlinear

non-Gaussian systems, and the filter degeneracy problem has hindered its application to real geophysical systems. At present, the main techniques for solving filter degeneracy are as follows (van Leeuwen *et al.*, 2019): (a) sample particles from a proposal density rather than from the original transition density (Ades and Van Leeuwen, 2013; Zhu *et al.*, 2016; Papadakis, 2007), (b) use a deterministic transformation process to move the prior particles to the

posterior particles (Reich, 2013), (c) calculate the particle weights locally (Poterjoy, 2016; Penny and Miyoshi, 2016; Farchi and Bocquet, 2018), and (d) combine particle filters with EnKFs or variational methods (Frei and Künsch, 2013; Morzfeld *et al.*, 2018).

In the localization framework inspired by the local particle filter (LPF) of Poterjoy *et al.* (2019), Chen *et al.* (2020) proposed the localized weighted ensemble Kalman filter (denoted as LWEnKF19 hereafter). The method first adopts the EnKF as the proposal density to obtain proposal particles and calculates proposal weights according to the prior particles and the observations. Then the local likelihood weights are calculated sequentially, and a merging step is used to update the particles according to the product of the likelihood weights and the proposal weights. Finally, optionally, particles are adjusted via a probability mapping approach.

The posterior particles obtained by the LWEnKF19 approximate the weighted ensemble Kalman filter (WEnKF: Papadakis *et al.*, 2010; Papadakis, 2007) near the observations, while retaining information from the EnKF and the proposal weights far from the observations. Experiments using the Lorenz 96 model show that it can combine some advantages of the EnKF and the LPF in both linear and nonlinear configurations. Meanwhile, experiments with the two-layer quasi-geostrophic model show its potential for real applications. However, the total weights may still be degenerate for high-dimensional real systems, since the proposal weights are calculated using the full model-error covariance matrix. The purpose of this article is to improve the LWEnKF19 for data assimilation in complex geophysical systems and then test the revised method in a real ocean model.

With one or more of the above techniques, some particle filters have been applied to real geophysical systems. The equivalent-weights particle filter (EWPF: Ades and Van Leeuwen, 2013; 2015) adopts a proposal density that depends on all particles at the previous time and ensures that most particles have the same weight. Browne and Van Leeuwen (2015) test the EWPF on a full-scale coupled ocean–atmosphere general circulation model with observing-system simulation experiments (OSSEs). Subsequent studies show that the performance of the EWPF is largely dependent on the nudging term between analysis steps (Browne, 2016).

With the idea of sequential-observation localization (Farchi and Bocquet, 2018), the LPF (Poterjoy, 2016; Poterjoy and Anderson, 2016; Poterjoy *et al.*, 2017) is used to assimilate artificial radar observations for the Weather Research and Forecasting (WRF) model. After some advances made to the LPF, Poterjoy *et al.* (2019)

compare the LPF with the ensemble adjustment Kalman filter assimilating real observations, which indicates the advantages of the LPF when nonlinear observation operators and nonlinear model processes are present. However, when the situation involves linear observation operators, linear models, and Gaussian errors, the LPF is at a disadvantage compared with the EnKF (Farchi and Bocquet, 2018).

As a hybrid method, the local ensemble Kalman particle filter (LEnKPF: Robert *et al.*, 2017) combines the EnKF and the PF as two stages; this has been implemented in the Consortium for Small-scale Modeling (COSMO) framework and assimilated real observations. The results indicate the potential of the LEnKPF for forecasting non-Gaussian variables.

The localized nonlinear ensemble transform filter (LNETF: Toedter *et al.*, 2016) is a second-order exact filter, which has been tested by OSSEs using the Nucleus for European Modelling of the Ocean (NEMO). The performance of the LNETF is comparable with that of the local ensemble transform Kalman filter (LETKF: Hunt *et al.*, 2015), but requires a longer spinup period.

The first particle filter implemented in the operational setup is the local adaptive particle filter (LAPF) proposed by Potthast *et al.* (2019). The LAPF is tested for the global ICOsahedral Nonhydrostatic (ICON) model at Deutscher Wetterdienst (DWD), and the score is lower than that of the LETKF. The PfVar is a hybrid algorithm with an idea similar to EnVar, which is also under investigation at DWD (van Leeuwen *et al.*, 2019). Details of the above PF applications are summarized in Table 1.

In this article, the LWEnKF19 is improved via localization of the proposal weights calculation. The revised method is tested in a weakly nonlinear system to verify whether the method can still maintain the advantages of the EnKF and the LPF in real applications. Variation in the ocean is a slowly changing process relative to that in the atmosphere. In addition, the observation operator used in ocean data assimilation is generally bilinear interpolation, which is a linear operator. Combining these considerations, ocean data assimilation is more suitable for testing the performance of assimilation methods in weakly nonlinear systems, which is difficult for particle filters, but advantageous for ensemble Kalman filters when the ensemble size is limited.

In section 2, we localize the proposal weights, extend the proposal weights to a vector, and present the modified method. A simple model test is conducted in section 3, before the application of the improved algorithm to ocean data assimilation with the Regional Ocean Modeling System (ROMS) in section 4. Discussions and conclusions are included in section 5.

TABLE 1 Configurations of PFs applied to real geophysical models

Algorithm	Model	Observation	N	
EWPF	HadCM3	SST	32	OSSE
	atmosphere component:	N_y=27,370		
	3.75°×2.5°×19 levels			
	ocean component:			
	1.25°×1.25°×20 levels			
	N_x=2,314,430			
LPF	WRF	Radar radial velocity and reflectivity	100	OSSE
	133×133 grid points ×40 levels			
LPF	WRF	Radar radial velocity and reflectivity	36	
	250×250 grid points ×51 levels	Oklahoma mesonet observations		
		cloud water path retrievals		
LETKPF	COSMO	Radar radial velocity and reflectivity	36	
	2.2km×2.2km×60 levels	radiosonde TEMP, wind, and humidity		
		wind profiler		
		SYNOP and ship surface pressure		
		aircraft temperature and wind		
LNETF	NEMO	SSH	120	OSSE
	0.25°×0.25°×11 levels	Argo temperature		
	N_x=333,234	N_y=3,273 on average		
LAPF	ICON	TEMP, PILOT, SHIP, SYNOP, BUOY	40	
	2,949,120 triangles × 90 levels	wind profiler, aircraft, AMV, radio occultations		
		scatterometer, satellite radiances		

2 | LOCALIZATION OF PROPOSAL WEIGHTS

In practical applications to high-dimensional models, calculating proposal weights using the full model-error covariance matrix in the LWEnKF will inevitably lead to filter degeneracy. Therefore, the proposal weights need to be localized. Consider the data assimilation at time step n. Assume that the dimension of model variables is N_x, the dimension of observations at time step n is N_y, and the number of particles is N. Similarly to the likelihood weights, we generalize the scalar full proposal weights w_i^* to the vector local proposal weights $w_{i,k}^*$ and attach to each model variable $x_{i,k}^n$ a proposal weight $w_{i,k}^*$, where i=1,2,…,N, k=1,2,…,N_x. We take $w_{i,k}^*$ as an example to illustrate how to calculate local proposal weights.

As shown in Figure 1, similarly to the state-domain localization mentioned in Farchi and Bocquet (2018), a circular (or spherical) region with the spatial position of $x_{i,k}^n$ as the centre and the radius of $2c^B$ is called the local block, which is denoted by B; the circular (or spherical) region

with the same centre position, but with a radius of $2c^D$, is called the local domain, denoted by D. When calculating the local proposal weight $w_{i,k}^*$, it is considered that only the model variables in the local block B and the observations in the local domain D have an influence on the local proposal weight.

The formulae for calculating the original full proposal weights are given in Appendix A of Chen *et al.* (2020). Similarly, in this article, the additive model error and the observation error are assumed to be white Gaussian. Considering localization, the local proposal weight is

$$w_{i,k}^* = \frac{p(\mathbf{x}_{i,B}^n|\mathbf{x}_{i,B}^{n-1})}{q(\mathbf{x}_{i,B}^n|\mathbf{x}_{i,B}^{n-1},\mathbf{y}_D^n)}. \quad (1)$$

Then the denominator of the proposal weight is modified as

$$q(\mathbf{x}_{i,B}^n|\mathbf{x}_{i,B}^{n-1},\mathbf{y}_D^n) \propto \exp\left[(\mathbf{x}_{i,B}^n - \mu_{i,B}^n)^{\mathrm{T}} \Sigma_{B,D}^{-1}(\mathbf{x}_{i,B}^n - \mu_{i,B}^n)\right], \quad (2)$$
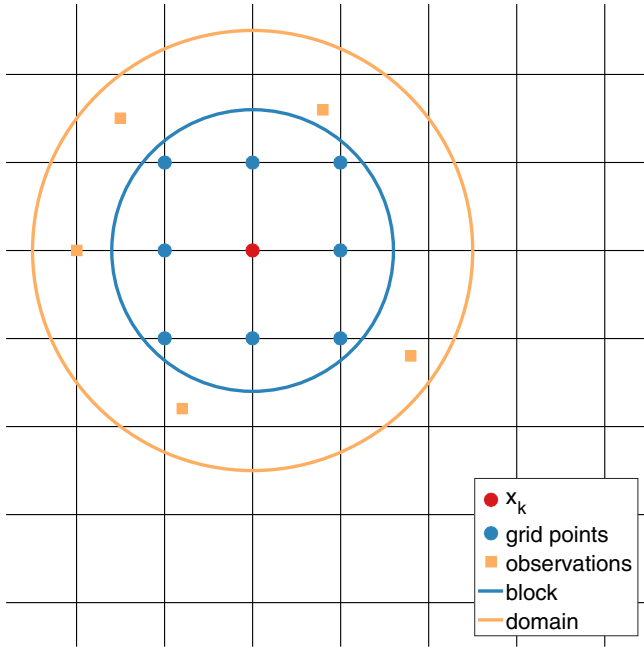
FIGURE 1 Schematic diagram of the local block and local domain. The red dot indicates the model variable $x_{i,k}^n$ corresponding to the proposal weight $w_{i,k}^*$. The blue dots are model variables and the yellow squares are observations. The part enclosed by the solid blue line is the local block, and the area enclosed by the yellow solid line is the local domain

where $\mathbf{x}_{i,B}^n$ represents the combined vector of the model variables $\mathbf{x}_i^n$ located in the local block B. $\mathbf{y}_D^n$ represents the vector formed by the observations $\mathbf{y}^n$ in the local domain D. The method to compute μ_i^n and Σ can be found in Chen *et al.* (2020), and the calculation of $\mu_{i,B}^n$ and $\Sigma_{B,D}$ also follows the same formulae, but the matrices used in the formulae are reduced to the local block or the local domain; see Equations A1 and A2.

Similarly, the numerator of the proposal weight (Equation 1) is

$$p(\mathbf{x}_{i,B}^n|\mathbf{x}_{i,B}^{n-1})$$
$$\propto \exp\left\{(\mathbf{x}_{i,B}^n - [M(\mathbf{x}_i^{n-1})]_B)^T \mathbf{Q}_B^{-1}(\mathbf{x}_{i,B}^n - [M(\mathbf{x}_i^{n-1})]_B)\right\}. \tag{3}$$

Here, M is the deterministic forecast model. The meaning of the subscript B of the vector $\mathbf{x}_i^n$ and $M(\mathbf{x}_i^{n-1})$ is the same as that for the vector $\mathbf{x}_i^n$ above. $\mathbf{Q}$ is the covariance matrix of the white Gaussian model error and $\mathbf{Q}_B$ is the principle submatrix of $\mathbf{Q}$ in the corresponding rows and columns.

As in Chen *et al.* (2020), the proposal weights (Equation 1) are also adjusted by a parameter $0 < \alpha < 1$:

$$w_{i,k}^* = (w_{i,k}^* - 1)\alpha + 1. \tag{4}$$

The parameter α actually sets a lower limit on proposal weights. In real applications, if the observation is an outlier or the bias of the forecast model is large, it may cause filter degeneracy, that is, the weights of a very small number of particles are particularly large, and the weights of most particles are very small and can be ignored. Therefore, the α adjustment is needed to prevent filter degeneracy effectively and enhance the robustness of the algorithm. Generally, the value of α is set to be slightly less than 1.

The LWEnKF19 also adjusts the likelihood weights with the coefficient α. Recently, Poterjoy *et al.* (2019) proposed an improved inflation method called β inflation, which is an observation-error inflation method that makes the weights reach the target effective size in the LPF. β inflation is also adopted to adjust the likelihood weights in the improved method. Otherwise, following Poterjoy *et al.* (2019), a mixing parameter $0 \le \gamma \le 1$ is introduced to modify the merging coefficients $r_{1,k}$ and $r_{2,k}$ (see Equations A17 and A18), which updates particles by combining the resampled current particles and resampled last-step particles in model state space, including at the location of observations. Choosing $\gamma < 1$ is helpful to alleviate filter degeneracy when the number of particles N is small. Meanwhile, similarly to the LPF, the revised algorithm uses kernel density distribution mapping (KDDM) as the probability mapping step, to compensate for the insufficiency of the merging strategy, which considered only the first two moments.

To ensure the clarity and completeness of the article, the details of the improved LWEnKF are provided in Appendix A. The derivation of formulae in Step 5 is similar to that in Chen *et al.* (2019). Please see Poterjoy *et al.* (2020) for details of the β inflation in Step 4 and the KDDM in Step 6.

3 | EXPERIMENTS IN THE LORENZ 96 MODEL

We compare the improved LWEnKF with the LWEnKF19 in a simple model – the 40-variable Lorenz 96 (L96) model (Lorenz, 2006). The differential equation for the model is

$$\frac{dx_k}{dt} = (x_{k+1} - x_{k-2})x_{k-1} - x_k + F, \tag{5}$$

where $k=1,2,\ldots,40$ and $x_{40+k}=x_k$, $x_{-k}=x_{40-k}$. F is the forcing term, which is set to 8.0 for the truth run and 8.4 for forecast to introduce model error. The time step is set to 0.05 (6 hr). The truth is generated by the truth run for 10,000 time steps. The observations are simulated from the

TABLE 2   Experiment design for the L96 model

Experiment	DA method	Localization parameter
ExptA	LWEnKF19	c
ExptB	LWEnKF	$c^D = c^B = c$
ExptC	LWEnKF	$c^D = c$, $c^B = 0$
ExptD	Control run	None

FIGURE 2   The average analysis RMSE over the data assimilation period of ExptA, ExptB, and ExptC as a function of ensemble size, in which the observation operators are (a) $h(x)=x$, (b) $h(x)=|x|$, and (c) $h(x)=\ln(|x|+1)$

truth by adding a random error drawn from $N(0, \mathbf{R})$, in which the observation-error covariance is $\mathbf{R} = \mathbf{I}$. The model variables at odd positions are observed every 24 hr (i.e., 4 time steps).

In fact, the parameters $c^B \geq 0$ and $c^D \geq 0$ of the improved LWEnKF can be chosen arbitrarily, so can be tuned in the experiments to get the best results. In practical applications, in order not to introduce additional localization parameters and not to increase computational cost for tuning, the cutoff parameter c of the likelihood weights is used as the value of c^D, that is, $c^D = c$. There are two artificial ways to determine B. One is to make $B = D$, that is, $c^B = c^D = c$. Another is to specify that B only contains $x_{i,k}^n$, that is, $c^B = 0$. Based on the above considerations, four experiments are conducted in this section. The first experiment uses LWEnKF19, the second and third experiments use the improved LWEnKF, but the localization parameter selection schemes are different, and the fourth experiment is the control experiment; these experiments are summarized in Table 2. The Gaspri–Cohn (GC) function is adopted as the localization function, for which the cutoff coefficient c is tuned from 1–20 grid points. The parameter α is chosen from range 0.70–1.00 experimentally. The motivation is to test the localization of proposal weights; the β inflation and γ mixing parameter are not used in this section.

Following Chen *et al.* (2020), we conduct the data assimilation experiments with three different types of observation operator: a linear function $h(x)=x$ and two nonlinear functions $h(x)=|x|$ and $h(x) = \ln(|x| + 1)$, in which the nonlinearity of the latter is stronger than the former. To consider sensitivity to the number of particles, the two methods are also tested with ensemble sizes of 10, 20, 40, 80, 160, and 320. All experiments were repeated 10 times to reduce the impact of random initial particles on results.

The analysis root-mean-square errors (RMSEs) in Figure 2 are averaged over 2,500 analysis cycles. The average RMSE of the control run (ExptD) at the corresponding time steps is 5.1972, which is too high to show in the figure. Compared with the control run, both methods have some improvements in the model variables. There is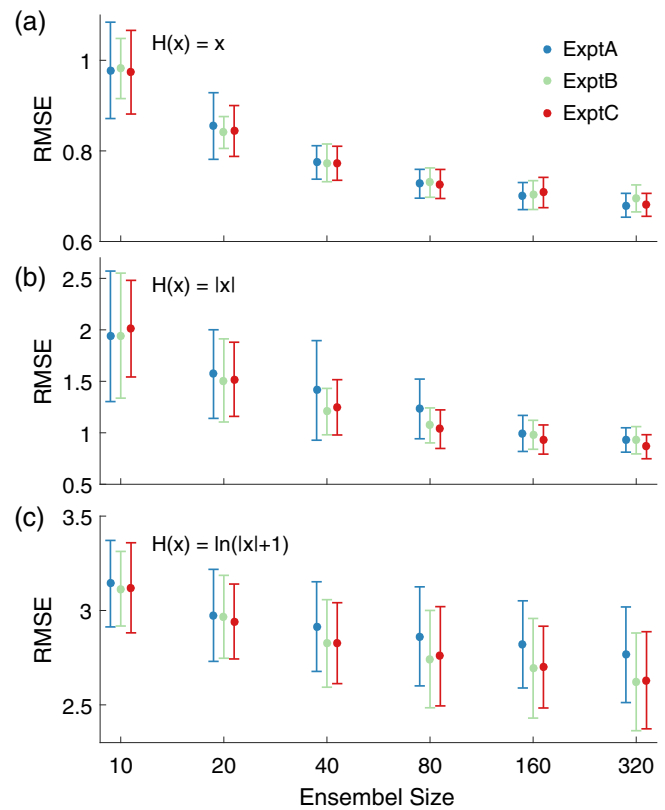 no filter degeneracy in all experiments. In the case of the linear observation operator, the three experiments do not show much difference; in the case of the stronger nonlinear observation operator, the two experiments (ExptB and ExptC) with the improved LWEnKF are obviously better than the original LWEnKF19 (ExptA). When the number of particles is small ($N=10, 20$), the performance of all DA experiments is not much different; when the ensemble size is large ($N \geq 40$), the two experiments (ExptB and ExptC) with localized proposal weights are not worse and sometimes even better than the LWEnKF19 (ExptA), especially in the case of stronger nonlinearity, where the advantage is obvious. In most cases, the RMSEs of ExptB and ExptC are similar, and sometimes the results of ExptC are superior to those of ExptB.

In order to study the effect of the localized proposal weights on the total weights of particles, the total weights of the model variable x_1 for the first 20 data assimilation cycles are shown in Figure 3. In this test, the observation operator is the absolute function and 80 particles are used. For comparability, the α parameters of ExptA, ExptB, and ExptC are set to 0.99, and the value of the localization parameter c of the three experiments is also the same.
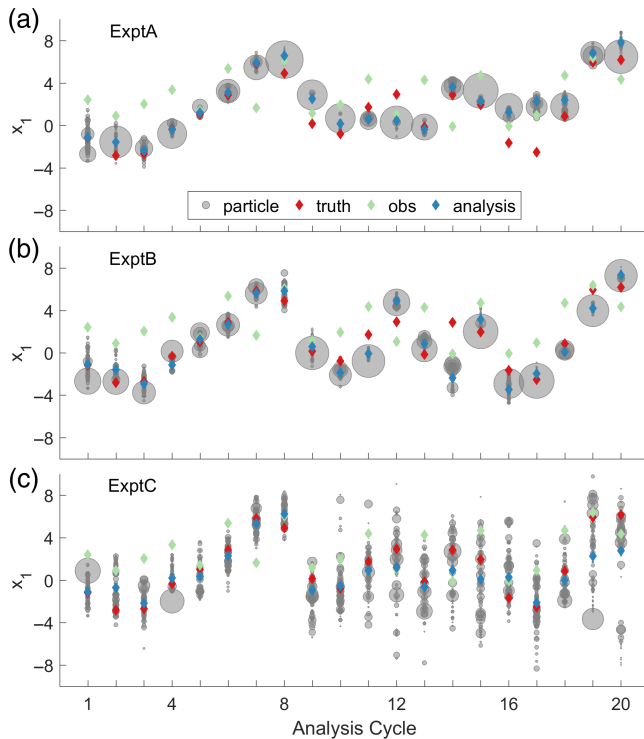
FIGURE 3 The total weights of particles in the first 20 analysis cycles for (a) ExptA, (b) ExptB, and (c) ExptC when α=0.99. The number of particles is 80, and the observation operator is $h(x)$ = |x|. The size of the grey circles indicates the value of the weights. The red, green, and blue diamonds represent the truth, observations, and mean of analysis particles, respectively

It can be seen clearly that the weights calculated by LWEnKF19 degenerate more severely, which means that the phenomenon in which a few particles concentrate most of the weight occurs frequently. The weights obtained by ExptB are slightly better than those of LWEnKF19, but at some analysis cycles the weights are still concentrated in a small number of particles. The weights calculated by ExptC are reasonable, and there is no occurrence in which a few particles occupy most of the weight. Moreover, the truth lies in the range of effective particles obtained by ExptC in all analysis cycles. This shows that, for ExptC, α=0.99 is sufficient to overcome the filter degeneracy. However, for ExptA and ExptB, it is obvious that α should be smaller.

In summary, experiments on the L96 model show that the average analysis RMSE of ExptC is not worse than that of the other two DA experiments under the case of three operators and different ensemble sizes. The weights calculated by ExptC are more reasonable, which means there is no need for too much manual adjustment. In addition, the local block of ExptC is smaller than that of ExptB, so the computational time of ExptC is also shorter, which is an important advantage in real applications.

4 | APPLICATION TO THE ROMS

In view of the various advantages of the LWEnKF with $c^D = c$ and $c^B = 0$, we test the scheme with the ROMS to explore its potential for application to ocean data assimilation further. For the sake of simplicity and no ambiguity, LWEnKF in this section refers to the LWEnKF with $c^D = c$ and $c^B = 0$, unless explicitly stated otherwise.

4.1 | Configuration for the ROMS

The ROMS is a free-surface, hydrostatic, primitive-equation regional ocean model with a topography-following coordinate (Shchepetkin and McWilliams, 2005; 2009). It has been widely used in various research and applications (Mu et al., 2019; Li and Toumi, 2017). The model region spans from 105–128°E and 15–24°N, which covers the northern South China Sea (SCS) and northwestern Pacific. The resolution of the model region is 1/6°×1/6° horizontally and 24 levels vertically. The bottom bathymetry is obtained from the NGDC's ETOPO2 (https://ngdc.noaa.gov/mgg/global/etopo2.html), which is a 2 argmin ×2 argmin resolution gridded data set. The model is forced by the three-hourly, 0.75°×0.75° resolution reanalysis atmosphere variables from the European Centre for Medium-Range Weather Forecasts (ECMWF) ERA-Interim (Dee et al., 2011), which contain the surface wind stresses, surface net heat flux, surface net freshwater flux, and solar shortwave radiation flux. The daily 1/12°×1/12° HYCOM reanalysis data (Metzger et al., 2014) are interpolated to the ROMS model grid as the initial and lateral boundary conditions.

4.2 | Data assimilation methods

The ROMS experiments are conducted on the National Center for Atmospheric Research (NCAR) data assimilation research testbed (DART: Anderson et al., 2009) to compare the LWEnKF improved by this article with the local perturbed EnKF (Anderson, 2003) and LPF (Poterjoy et al., 2019). Sequential observation localization is required by all three filters. The cutoff coefficient c (half of the localization radius) is determined by tuning from 0.003–0.03, which is roughly equivalent to a horizontal localization radius of 36–366 km. The EnKF uses adaptive prior multiplicative inflation, as described in Anderson (2007). A control run, which did not assimilate any observations, is also presented for comparison.

The LPF adopts β inflation, the mixing parameter γ, and the KDDM proposed in Poterjoy et al. (2019). Similarly, β inflation, the mixing parameter γ, and the KDDM are

used by the LWEnKF, as stated in section 2. Meanwhile, the parameter α is also used for adjusting the proposal weights in the LWEnKF. The parameters α and γ are both in [0,1], and they are generally slightly less than 1. To reduce the cost of tuning parameters, we set $\alpha=\gamma$ in the LWEnKF experiments in this section. The target effective sample size and the parameter γ for the LPF and LWEnKF are chosen experimentally within range 0.70–0.999. Note that a running product of many small numbers may lead to underflow errors, so for both the LPF and LWEnKF we calculate a running sum of the logarithms of the local likelihood weights for the calculation of the total weights in Equation A11 instead.

In addition, the model error variance is required in the calculation of the proposal weights for the LWEnKF (see Equations 3 and A1). Several methods to estimate the model-error covariance have been developed (Zhu et al., 2018; Todling, 2015a; 2015b). Following Browne and Van Leeuwen (2015, 2015b), we assume that the variance of a long model run is related to the variance of the model error. The model runs for 10 years, from 2007–2016, where the first year is removed as the spinup period. Then, the model error variance is approximated by the daily variance in the model over the nine0-year run.

The data0 sets used in the assimilation are the 1/4° gridded daily sea-surface temperature (SST) data from the Advanced Very High Resolution Radiometer (AVHRR), the 1/4° gridded daily sea-surface height (SSH) data from Archiving, Validation and Interpretation of Satellite Oceanographic Data (AVISO) and the quality-controlled ocean temperature and salinity profiles from the Met Office Hadley Centre EN4 data set (Good et al., 2013). The along-track SSH and SST are preferable above the gridded product, because the observation errors are less dependent. However, to avoid the introduction of additional error or bias due to observation quality, the gridded SSH and SST are considered in assimilation experiments in this article.

The assimilation window is chosen to be 4 days, which is slightly shorter than the 5 days used in some literature (e.g., Kerry et al., 2018; Li and Toumi, 2017). This choice is based mainly on two considerations: First, the assimilation window is short, to ensure that the model variability is small; second, the gridded surface observation data are considered in the experiments, so there is no need to get enough observations through a long window. Observations are considered to be available at the middle of the assimilation window. In a window, the assimilated observations are as follows: gridded SST and SSH observations at the assimilation time, and all the temperature and salinity profiles within ±2 days of the assimilation time. The total duration for assimilation cycles is 124 days, from October 1, 2015–February 2, 2016.

The dimension of the model variables is 790,745 and the average number of observations processed per analysis step during the assimilation period is 4,803. Considering the degrees of freedom of the model variables and observations, as well as the limitation of computational resources, the number of particles is chosen to be 50.

Following Hoteit et al. (2013), the initial ensemble is generated by an exact second-order sampling scheme (Pham, 2001). An empirical orthogonal function (EOF) analysis is used to find the dominant variability from the nine-year run model states. Then, the initial particles are given by the following equation:

$$\mathbf{x}_i = \bar{\mathbf{x}} + \sqrt{N}\mathbf{L}\mathbf{r}_i^{\mathrm{T}}, \qquad (6)$$

where $\mathbf{L}$ is a matrix with columns consisting of $N-1$ EOFs, $\bar{\mathbf{x}}$ is the mean of the nine-year model states, $\mathbf{r}_i$ is the ith row of a $N\times(N-1)$ random matrix, the columns of the matrix are orthogonal, and the sum of the columns is 0. The initial ensemble has mean $\bar{\mathbf{x}}$ and covariance $\mathbf{L}\,\mathbf{L}^{\mathrm{T}}$, which is the best approximation of the nine-year model states (Hoteit et al., 2013).

In order to increase the spread of the prior ensemble during the assimilation period, the atmospheric forcing variables of each month are also perturbed in a similar way to that in Li and Toumi (2017):

$$\mathbf{f}_i = \mathbf{f} + 0.2\sqrt{N}\mathbf{L}^{\mathrm{f}}\mathbf{r}_i^{\mathrm{T}}. \qquad (7)$$

Only the surface wind stresses and surface net heat flux are perturbed, and their error is assumed to be 20%. The EOFs in the matrix $\mathbf{L}^{\mathrm{f}}$ are extracted from the nine-year ECMWF ERA-Interim data for the corresponding month.
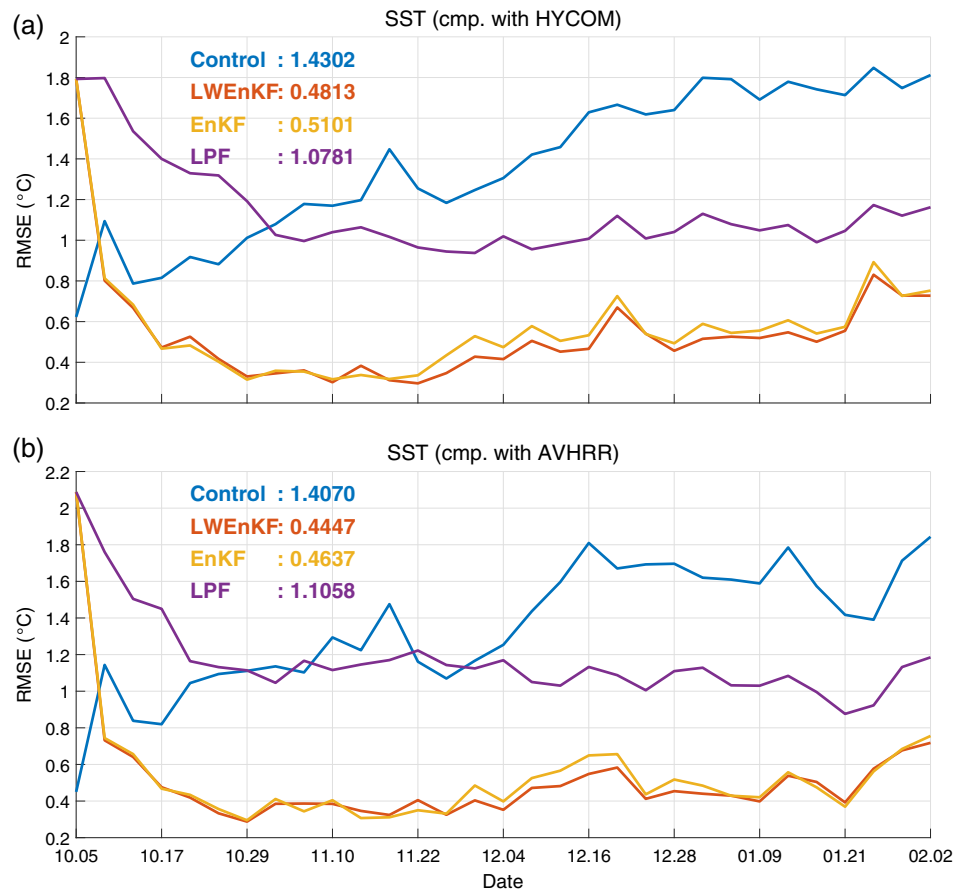
4.3 | Results

4.3.1 | RMSE and spread

In order to compare the LWEnKF accurately with the EnKF and the LPF, the RMSE is used to assess forecasts during the assimilation period in this section. Since we are concerned about the northern part of the South China Sea and do not care about the mainland coast, runoff is not considered in the model. Therefore, in the spatial average RMSE, the area with a water depth of less than 60 m on the mainland coast is not taken into account. The four-day forecast that is projected on to observation space to calculate the RMSE is the mean of 50 prior particles.

Figure 4 shows the spatial mean RMSE at each analysis step between the HYCOM reanalysis data or AVHRR observations and the prior SST obtained by the three

FIGURE 4 Spatial averaged four-day forecast RMSE of SST at each analysis step for the control run (blue line), LWEnKF (red line), EnKF (yellow line), and LPF (purple line), computed with (a) HYCOM and (b) AVHRR data. The values in the left upper corner denote the time-averaged RMSE of the three methods, excluding the spinup period

filters. The corresponding RMSE of the control run without assimilation of any observations is also illustrated. Compared with the reanalysis data or the observations, the RMSE of the control run increases with time. At the beginning of the assimilation cycles, the RMSE of the three methods is larger than the control. There is a significant decrease in the subsequent spinup period, and then the RMSE remains at a relatively stable level. The results before October 17 are removed as spinup, and are not included in the time-averaged RMSE shown in the upper left corner of Figure 4. All three filters have played a role in improving the forecast. However, the LPF results are obviously worse than the other two methods. Although the overall trend of the RMSE time series of the LWEnKF is not much different from that of the EnKF, it is still an improvement from the perspective of time-averaged RMSE, compared with the EnKF. Compared with the AVHRR gridded data, the averaged error of the SST is reduced by 68.05% by the LWEnKF, and 67.04% and 20.35% by the EnKF and LPF, respectively.

The temporal evolution of the spatial mean RMSE computed between the SSH forecasts and the HYCOM or AVISO data is illustrated by Figure 5. Since the mean of the initial particles is not very different from the observations or reanalysis data, the spinup period is not

obvious. Compared with the HYCOM or AVISO data, the time series of the control run and the LPF are very consistent, which shows that the LPF has a limited effect in improving SSH. The time series of the LWEnKF and the EnKF are similar, and there are obvious improvements compared with the control. To maintain the consistency of the RMSE, the spinup period is also subtracted from the time-averaged RMSE in the upper right corner of Figure 5. Compared with the AVISO observations, the error decreased from 16.15 cm in the control run to 7.64 cm for the LWEnKF, 7.98 cm for the EnKF, and 15.85 cm for the LPF on average, with each experiment reducing error by 52.69%, 50.59%, and 1.86%, respectively.

In order to compare the three filters more clearly, the RMSE time series in Figures 4b and 5b are used to draw a box plot, as shown in Figure 6a,b, respectively. Obviously, the RMSE of the LPF is significantly different from the other two methods, since the main body of the box obtained by the LPF does not overlap with that of the other two filters. The median of the LWEnKF is slightly smaller than that of the EnKF. However, the notches in the box plot of the LWEnKF and the EnKF overlap; there is not confidence that the true median of the RMSE time series resulting from the two is different. In addition, the box of
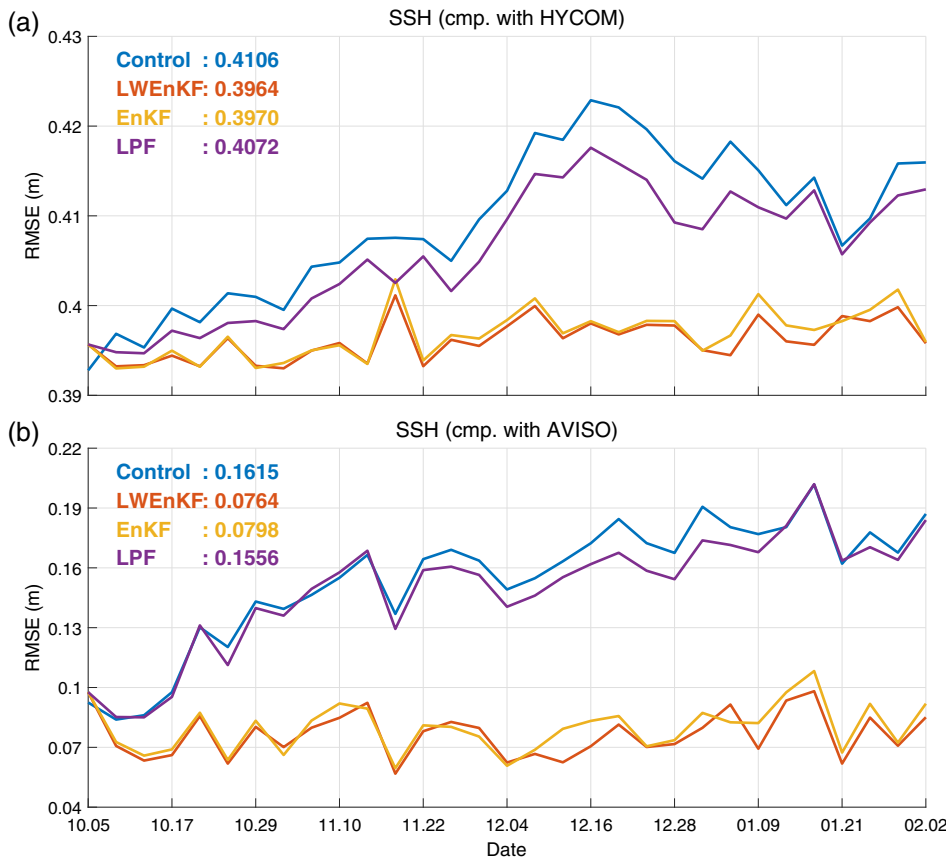
(a) SSH (cmp. with HYCOM)

Control : 0.4106
LWEnKF: 0.3964
EnKF   : 0.3970
LPF   : 0.4072

(b) SSH (cmp. with AVISO)

Control : 0.1615
LWEnKF: 0.0764
EnKF   : 0.0798
LPF   : 0.1556

FIGURE 5 Spatial averaged four-day forecast RMSE of SSH at each analysis step for the control run (the blue line), LWEnKF (the red line), EnKF (the yellow line), and LPF (the purple line), computed with (a) HYCOM and (b) AVISO data. The values in the left upper corner denote the time-averaged RMSE of the three methods, excluding the spinup period

the LWEnKF is slightly shorter than that of the EnKF, but it is difficult to calculate the uncertainty in the RMSE, as only 50 particles are used.

The ratios of the RMSE and spread of SST and SSH are also illustrated in Figure 7a,b, respectively. The RMSE of the LPF is too large, resulting in an excessive ratio. Both the LWEnKF and the EnKF have a certain degree of under-dispersion, while the LWEnKF is the least underdispersive of the three filters.

Ocean surface currents from the Global Drifter Project (GDP) data during period October 17, 2015–February 02, 2016 are also used to provide independent validation. The averaged RMSEs between the forecast currents of the three filters and those of drifters are summarized in Table 3. The performance of the LWEnKF is the best among all three DA methods. Compared with the control run, the LWEnKF reduces the error by 29.90% and 20.58% for u and v, respectively.

To verify the adjustment of the assimilation to the model variables at the subsurface and deep ocean, the Argo temperature and salinity profiles of EN4 data set are employed for validation. Figure 8 shows the average RMSE of prior temperature and salinity of the LWEnKF, EnKF, and LPF experiments for the upper 2,000 m. The RMSE curves of the temperature obtained by the three methods are very similar (Figure 8a). Although the average salinity

RMSE of the LWEnKF is also the smallest, the difference in RMSE between the three methods at different depths is relatively large. On the one hand, the number of salinity observations is much less than the number of temperature observations (including SST and temperature profiles), which leads to limited assimilation performance of the salinity. On the other hand, the salinity is also affected by temperature observations, while the three methods are different in dealing with the relationship between temperature and salinity. These are some of the reasons why the RMSE curves of salinity obtained by the three filters vary widely.

4.3.2 | Surface states

In order to qualitatively and intuitively investigate the characteristics of the LWEnKF further, the Ocean Surface Current Analysis Reat-time (OSCAR: Bonjean and Lagerloef 2002) currents are used for comparison with the four-day forecast of the assimilation analysis. The OSCAR product provides 1/3°×1/3° global surface currents averaged over the top 30 m of the upper ocean using satellite SSH, wind, and temperature. Despite the lack of more complex physical processes, OSCAR can provide direct satellite measurements of surface currents on a fixed

FIGURE 6 Box plot of the RMSE of (a) SST and (b) SSH for the LWEnKF, EnKF, and LPF, computed with (a) AVHRR and (b) AVISO data, respectively
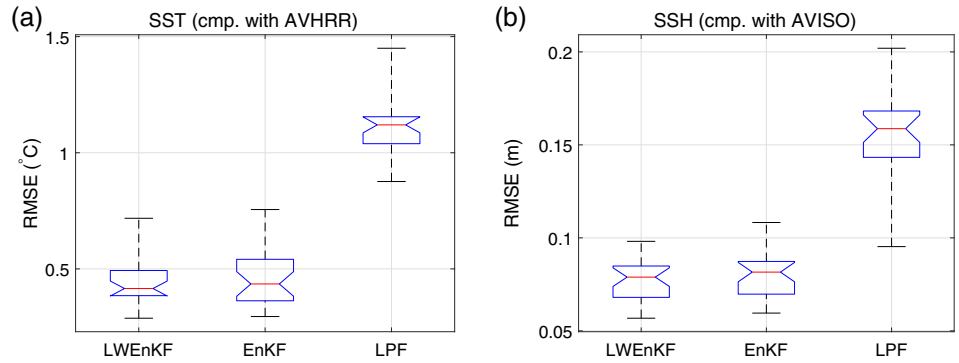

FIGURE 7 Spatial averaged four-day forecast RMSE/spread of (a) SST and (b) SSH at each analysis step for the LWEnKF (red line), EnKF (blue line), and LPF (yellow line), computed with the (a) AVHRR and (b) AVISO data. The values on the right show the time-averaged RMSE/spread of the three methods, excluding the spinup period
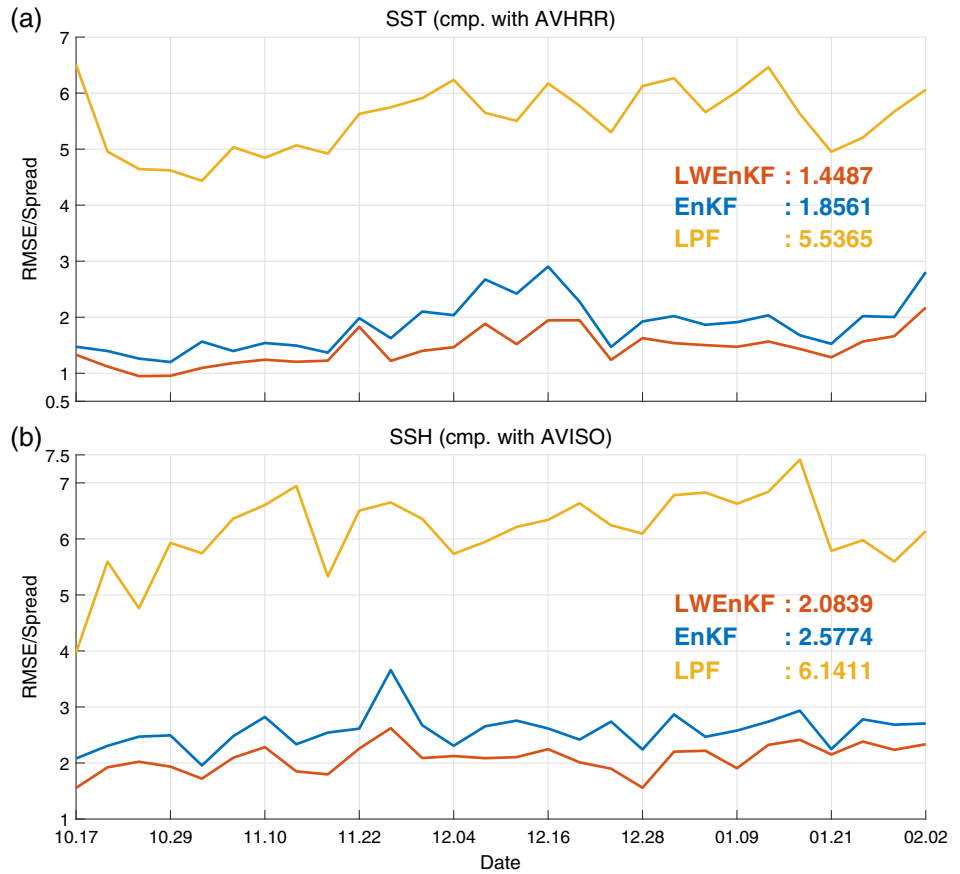

TABLE 3 Averaged four-day forecast RMSE of 15-m currents compared with drifter data.

	LWEnKF	EnKF	LPF	Control run
u (cm·s^{-1})	19.9624	20.5015	24.2599	28.4786
v (cm·s^{-1})	19.6250	20.0270	24.3808	24.7090

global grid at fixed time intervals (Dohan and Maximenko, 2010).

Figure 9 shows the spatial pattern of surface currents and SSH for four selected days, during which an anti-cyclonic eddy is observed in the OSCAR dataset in the southwest of Taiwan on November 10, 2015 and propagates southwestward along the continental slope to the

southeast of Hainan. In Figure 9d for the LPF experiment, the forecasts deviated completely from the OSCAR current and AVISO SSH in Figure 9a. Compared with Figure 9a, the SSH forecasts from the LWEnKF and EnKF experiments in Figure 9b capture the spatial pattern, but their SSHs are lower in the centre of anticyclonic eddies and the continental coast. In the forecast currents of the LWEnKF,
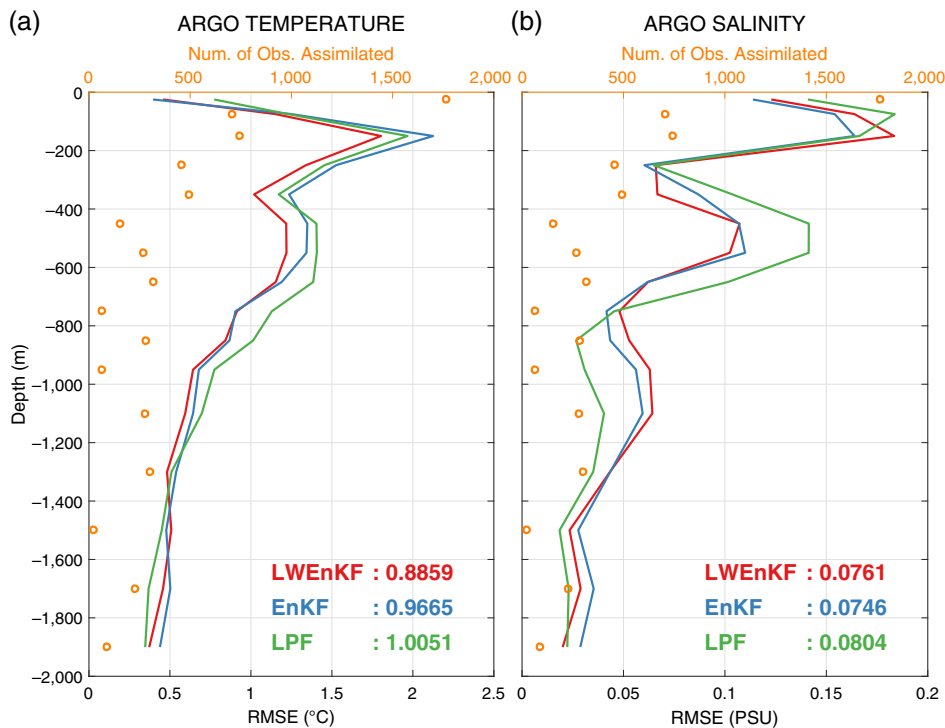
FIGURE 8 Averaged four-day forecast RMSE at every level of (a) temperature profiles and (b) salinity profiles for the LWEnKF (red line), EnKF (blue line), and LPF (green line), computed with EN4 Argo data. The values in the right bottom corner denote the vertical averaged RMSE of the three methods, excluding the spinup period. The orange coordinate and circles show the number of observations of the corresponding kind that are assimilated over the total assimilation duration

it can be clearly seen that an anticyclonic eddy propagates from the southwest of Taiwan on November 10, 2015 to the southeast of Hainan on January 9, 2016, while this eddy is not produced in the forecast currents of the EnKF on January 9, 2016.

A geometry-based eddy detection algorithm proposed by Nencioli *et al.* (2010) is employed to evaluate the eddy forecast capability of the three filters. The algorithm detects eddies based exclusively on the geometry of the velocity vector, which can also indirectly validate whether the forecast currents are consistent with the geometry of the velocity of the OSCAR data. The currents and eddies detected on January 9, 2016 are presented in Figure 10. In the LWEnKF run in Figure 10b, both anticyclonic eddies are predicted, but the scale of the eddy in the southwest of Taiwan is too large; a cyclonic eddy in the middle is also captured, where a larger eddy combined with a smaller eddy is observed in OSCAR dataset; additionally, there is a cyclonic eddy in the south of Hainan, but the eddy provided in OSCAR is in the southeast of Hainan. The EnKF produces only one anticyclonic eddy in the southwest of Taiwan, which is also too large in scale. The currents obtained by the LPF are greatly different from those of OSCAR, which is unreasonable.

Comparison with OSCAR data may not be sufficient to verify the velocity field, because the OSCAR currents are mainly geostrophic and there is no error estimate. No. 61504350 drifter was affected by the anticyclonic eddy in the southwest of Taiwan, moving southwestward from

December 2015–January 2016. Figure 11 compares the ocean surface currents predicted by the LWEnKF, EnKF, and LPF with the No. 61504350 drifter trajectory. The core of the anticyclonic eddy of the LWEnKF is more eastward than that of the EnKF on January 5, 2016, so that the drifter can be captured by the south edge of the eddy core in LWEnKF and move northwestward. On January 13, 2016, the drifter is on the south edge of the eddy core of the LWEnKF, but on the northeast edge of the eddy core of the EnKF, which indicates that the velocity field is more reasonable in the LWEnKF. The velocity field of the LWEnKF is closer to the No. 61504350 trajectory than that of the EnKF, and the LPF fails to reproduce the anticyclonic eddy at the surface.

The SST departures between the AVHRR gridded data and the four-day forecasts of the LWEnKF, EnKF, and LPF are given in Figure 12. The performance of the LPF is the worst among the three filters. The prior errors of the LWEnKF have a similar pattern to those of the EnKF, and are slightly smaller than those of the EnKF in some areas. Note that on December 20, 2015 there are large errors in the northwest of Luzon. According to the daily AVHRR gridded data, the northwestern coast of Luzon began to cool down during December 17–20, from about 25 °C on December 16 to about 21 °C on December 20, and the SST recovered to about 24 °C on December 21 (not shown here). The prior SST on December 20 is predicted from the analysis state on December 16, so this cooling process was not reflected by the model, resulting in large errors in the northwest of Luzon on December 20, 2015 in Figure 12a,b.
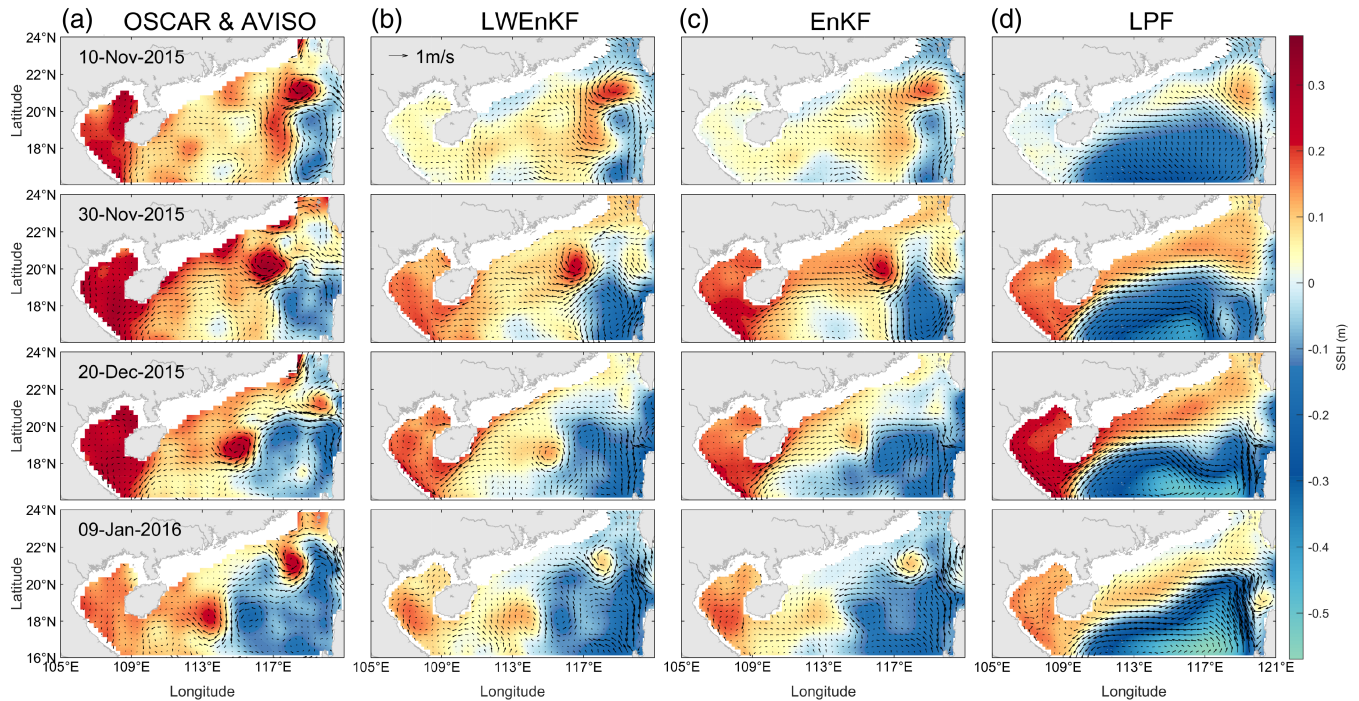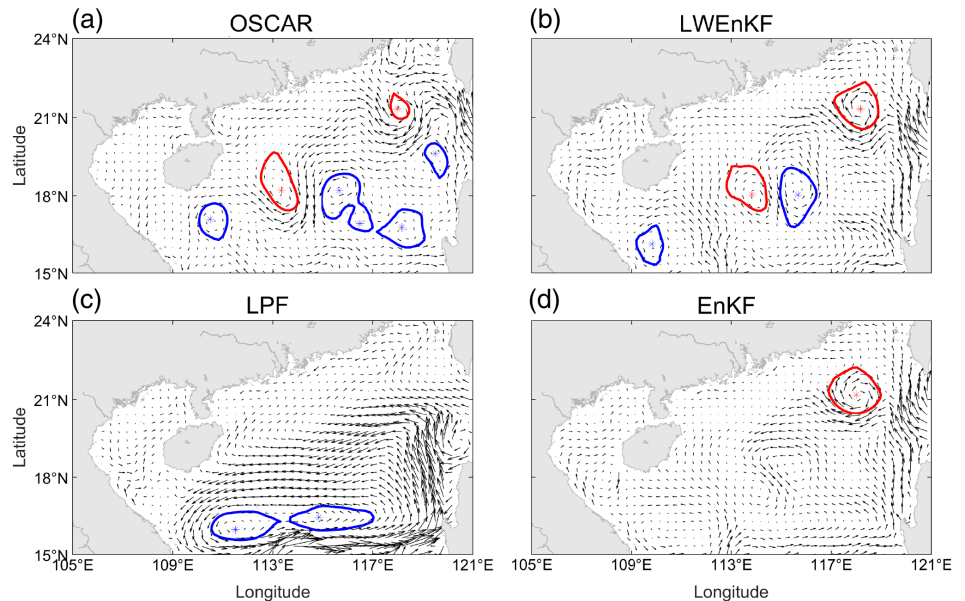
FIGURE 9 The SSH (shading) and surface currents (arrows) of (a) AVISO and OSCAR data, (b) LWEnKF, (c) LPF, and (d) EnKF. The rows represent the date of selection every 20 days to highlight the propagation of the mesoscale eddy

FIGURE 10 The surface currents (arrows) of (a) OSCAR data, (b) LWEnKF, (c) LPF, and (d) EnKF on January 9, 2016. The red closed curves represent anticyclonic eddies and the blue closed curves represent cyclonic eddies. The asterisks are the centres of the eddies

4.3.3 | Computational costs

The computational time spent by the LWEnKF, EnKF and LPF in the first analysis step is also tested for 10 times. The total number of observations assimilated in this step is 4,821. Since the localization radius affects the computational time, the cutoff is set to 0.02 for all three filters in this subsection. The hardware used in the experiments is Intel Xeon CPUs. There are 16 cores with 64 GB usable memory per node.

As described in section 2, the LWEnKF first uses the local perturbed EnKF to assimilate the observations, then calculates the local proposal weights, and finally computes the local likelihood weights and performs the merging step and KDDM step like the LPF. In theory, the complexity of the LWEnKF is constructed of three parts. One part is the
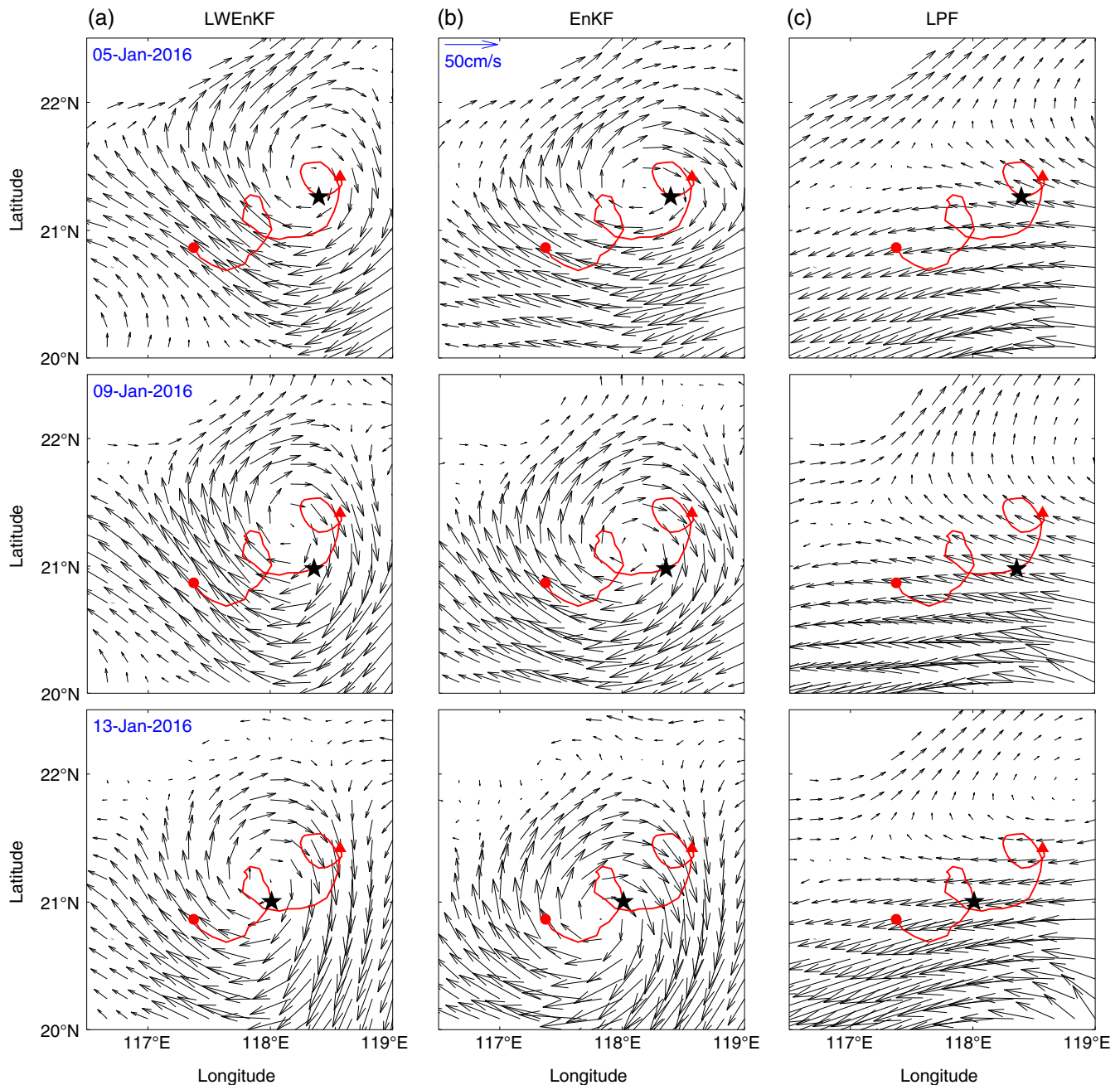
FIGURE 11 The velocity field (arrows) at 15 m for the four-day forecast of (a) LWEnKF, (b) EnKF, and (c) LPF. The rows represent the date of selection every 4 days. The No. 61504350 drifter trajectory is represented by the red curves, the position of the drifter on January 3, 2016 is represented by the triangle, the position on January 15, 2016 is represented by the circle, and the pentagram denotes the location on the selected date

complexity of the EnKF, which can be found in Tippett *et al.* (2003). One part is the complexity of calculating the proposal weights as described in Step 2 in section 2. The last part is the complexity of the LPF, which is studied in Farchi and Bocquet (2018).

The computational time in Figure 13 shows that, if parallelism is not used, the LPF takes almost three times as long as the EnKF, while the LWEnKF spends only slightly longer than the LPF. The computational time

includes the input and output time. Meanwhile, in the LWEnKF, the localization initial calculation for finding close model variables or observations need only be performed once. With more cores used, the computational times of the LWEnKF and LPF become closer to that of the EnKF.

Compared with the EnKF, the LPF requires extra memory $N_x \times N$ to store the likelihood weights. In addition to such requirements, the LWEnKF also needs a memory
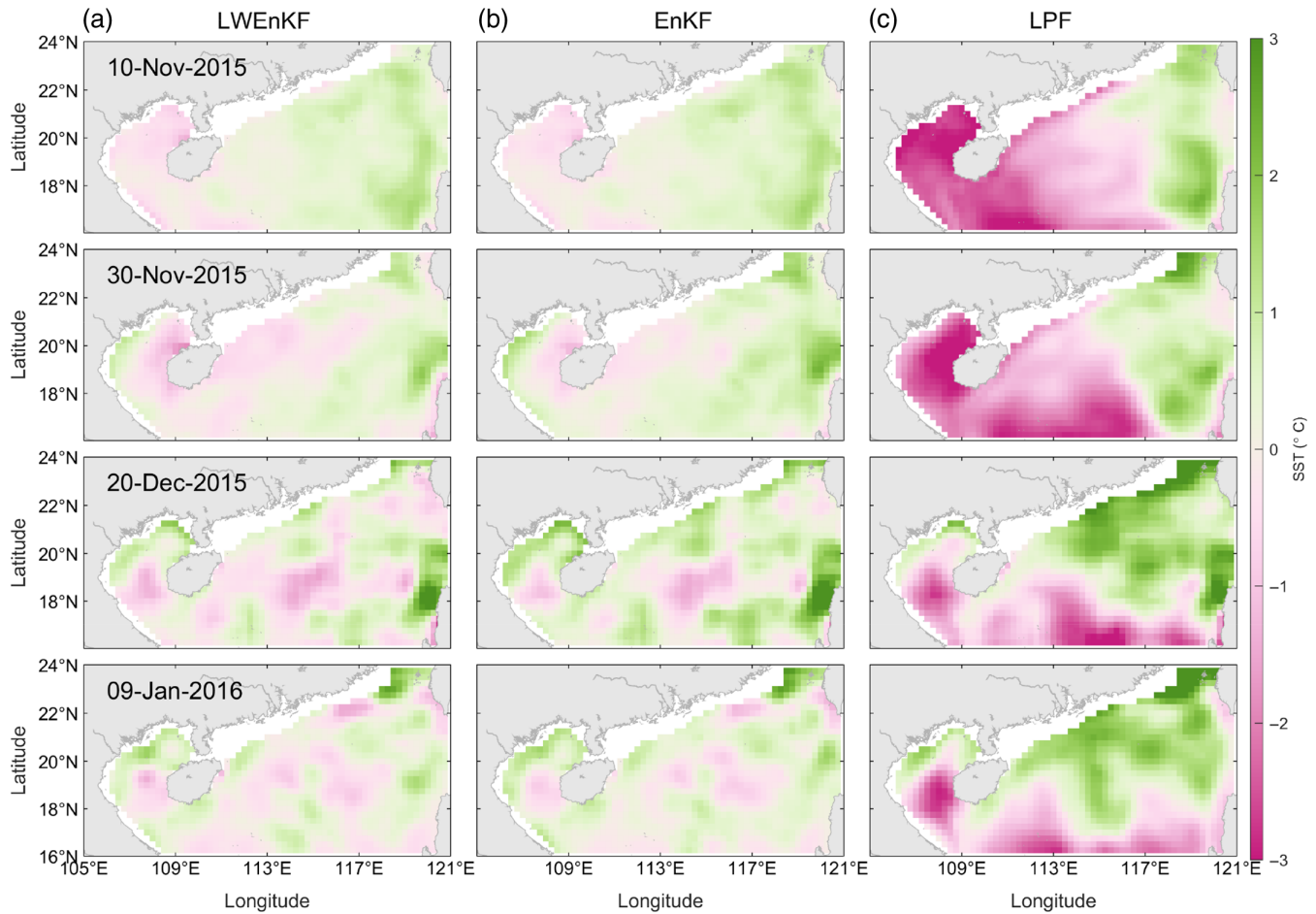
FIGURE 12 The SST departures between the AVHRR data and the four-day forecasts of (a) LWEnKF, (b) EnKF, and (c) LPF. The rows represent the date of selection every 20 days

$N_x \times N$ to store the proposal weights. Such a cost is respectively about twice or three times that of the EnKF, considering that the ensemble size is typically of the order of tens or hundreds.

5 | DISCUSSION AND CONCLUSIONS

Chen *et al.* (2020) proposed a local particle filter with the EnKF as proposal density, denoted by LWEnKF19 in this article. They also compared the LWEnKF19 with the EnKF and the LPF in simple models, and conclude that the LWEnKF19 can combine the advantages of the EnKF and LPF and has good performance in both linear and nonlinear configurations. The motivation of this article is to improve the proposal weights calculation in LWEnKF19, and compare the modified LWEnKF with the EnKF and LPF in mildly nonlinear real systems to check whether the LWEnKF can still work well in real applications. First, the original LWEnKF19 is improved via calculating proposal

weights locally, so that the revised LWEnKF can be applied to real atmosphere or ocean data assimilation without filter degeneracy. Then, a weakly nonlinear real ocean system is used to compare the revised LWEnKF with the EnKF and LPF.

When local proposal weights are calculated, two localization parameters c^B and c^D are introduced, which correspond to the localization half-radius for the local block and local domain, respectively. In order not to increase the cost of tuning parameters, the localization parameter c^D is selected to be equal to the localization parameter c of the original algorithm. That is, only those observations within $2c$ of the model state x_k will have an impact on its proposal weight. Two choices for the localization radius for the local block are tested in the L96 model. One is $c^B=c$, which takes into account the correlations of model error locally. Another is $c^B=0$, which only considers the variance of model error when the proposal weights are calculated. The LWEnKF19 is compared with the modified algorithm with the two choices of c^B. The RMSE resulting from the L96 experiments shows that the performance of the three
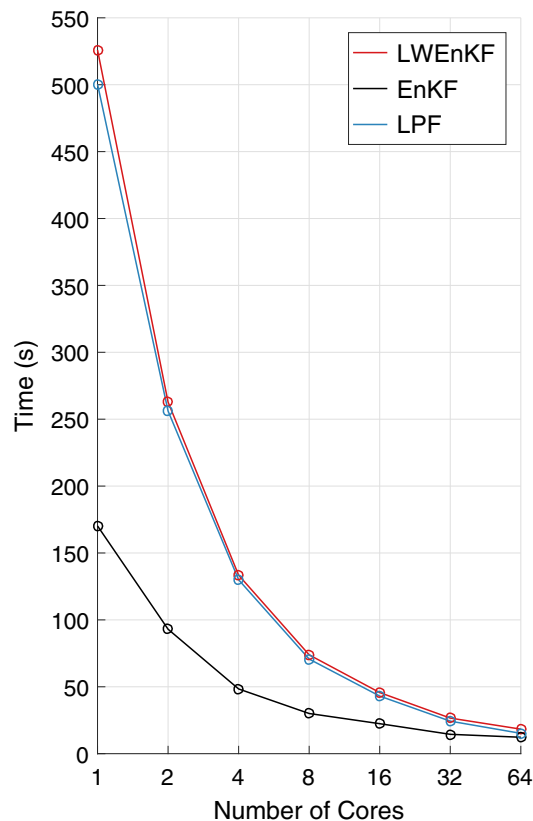
FIGURE 13 Total computational time for one analysis step of the LWEnKF, EnKF, and LPF

is not very different when ensemble size is relatively small. As the number of particles increases, both schemes of the revised filter have lower RMSE than the original algorithm when the observation operators are nonlinear. Considering that the weights obtained by the LWEnKF with $c^B = 0$ are more reasonable than those for the other two filters, and the computational time is less than for the scheme with $c^B = c$, this choice is thought to be more suitable for real model applications.

Ocean data assimilation experiments with ROMS at DART show the potential of the LWEnKF for real applications. Comparisons between the LWEnKF, EnKF, and LPF are performed in view of RMSE, spread, surface states, and computational cost.

Spatial or temporal averaged RMSE of the SST, SSH, and Argo profiles shows that the LWEnKF performs a little better than the EnKF, though we do not have confidence in this, since the notches in the box plot of the LWEnKF and the EnKF overlap. The ratio of RMSE and the spread of the SST and SSH indicates that the LWEnKF is the least underdispersive among the three filters. The forecast SST bias of the LWEnKF and the EnKF is comparable. However, for the surface current, the forecast of the LWEnKF is obviously more reasonable than that of the EnKF. For observed variables, the observation operators are linear in

the experiments, so the EnKF is good enough to estimate the posterior state, and the LWEnKF provides no measurable advantage; for unobserved variables, the EnKF approximates them by covariance, while the LWEnKF can estimate higher-order moments via attaching each particle with weight to obtain a more accurate posterior.

The LPF ensemble does not converge to the observed solution in an ample amount of time. There may be two reasons. One is that the LPF is not as efficient as data assimilation methods with linear/Gaussian assumptions when dealing with linearity(weak nonlinearity)/Gaussianity, which has been verified by simple model tests (Chen *et al.*, 2020; Farchi and Bocquet, 2018). Another possible cause is the inappropriate initial particles. The LPF does not change the value of particles directly, but calculates weights for each particle according to the likelihood function, then adjusts the value of particles based on the weights. If the initial particles deviate greatly from the truth, these particles are not important when representing PDFs, and the true likelihood for them should be small. Nevertheless, what matters is the relative importance of the particles after normalization, so the particles cannot describe PDFs accurately. Therefore, we speculate that the LPF requires a higher quality of initial particles than the LWEnKF or EnKF, which is under investigation.

Additionally, we also compare the computational cost of the three filters, which depends largely on the implementation of the DART. The computational time of the LWEnKF is much larger than that of the EnKF, but only a little greater than that of the LPF, which is affordable in the ocean data assimilation experiments in this article. The memory requirements of the LWEnKF and LPF are about twice and three times those of the EnKF, respectively.

In conclusion, the LWEnKF has a performance comparable to or even better than that of the EnKF in the mildly nonlinear ocean system, which is consistent with the results in simple models by Chen *et al.* (2020). In the future, we will test the LWEnKF in a stronger nonlinear real system. Such a system is more advantageous for particle filters, thus verifying fully whether the LWEnKF can still combine the advantages of the EnKF and the PF in real applications.

ORCID
Yan Chen https://orcid.org/0000-0003-2066-6064

REFERENCES

Ades, M. and Van Leeuwen, P.J. (2013) An exploration of the equivalent weights particle filter. *Quarterly Journal of the Royal Meteorological Society*, 139(672), 820–840. https://doi.org/10.1002/qj.1995

Ades, M. and Van Leeuwen, P.J. (2015) The effect of the equivalent-weights particle filter on dynamical balance in a primitive equation model. *Monthly Weather Review*, 143(2), 581–596. https://doi.org/10.1175/MWR-D-14-00050.1

Anderson, J., Hoar, T., Raeder, K., Liu, H., Collins, N., Torn, R. and Avellano, A. (2009) The data assimilation research testbed a community facility. *Bulletin of the American Meteorological Society*, 90(9), 1283–1296. https://doi.org/10.1175/2009bams2618.1

Anderson, J.L. (2003) A local least squares framework for ensemble filtering. *Monthly Weather Review*, 131(4). https://doi.org/10.1175/1520-0493(2003)131%3C0634:ALLSFF%3E2.0.CO;2

Anderson, J.L. (2007) An adaptive covariance inflation error correction algorithm for ensemble filters. *Tellus Series A – Dynamic Meteorology and Oceanography*, 59(2), 210–224. https://doi.org/10.1111/j.1600-0870.2006.00216.x

Bonjean, F. and Lagerloef, G.S.E. (2002) Diagnostic model and analysis of the surface currents in the tropical Pacific Ocean. *Journal of Physical Oceanography*, 32(10), 2938–2954. https://doi.org/10.1175/1520-0485(2002)032<2938:dmaaot>2.0.co;2

Browne, P.A. (2016) A comparison of the equivalent weights particle filter and the local ensemble transform Kalman filter in application to the barotropic vorticity equation. *Tellus Series A – Dynamic Meteorology and Oceanography*, 68(1), 30466. https://doi.org/10.3402/tellusa.v68.30466

Browne, P.A. and Van Leeuwen, P.J. (2015) Twin experiments with the equivalent weights particle filter and HADCM3. *Quarterly Journal of the Royal Meteorological Society*, 141(693), 3399–3414. https://doi.org/10.1002/qj.2621

Chen, Y., Zhang, W. and Zhu, M. (2020) A localized weighted ensemble Kalman filter for high-dimensional systems. *Quarterly Journal of the Royal Meteorological Society*, 146(726), 438–453. https://doi.org/10.1002/qj.3685

Dee, D.P., Uppala, S.M., Simmons, A.J., Berrisford, P., Poli, P., Kobayashi, S., Andrae, U., Balmaseda, M.A., Balsamo, G., Bauer, P., Bechtold, P., Beljaars, A.C.M., van de Berg, L., Bidlot, J., Bormann, N., Delsol, C., Dragani, R., Fuentes, M., Geer, A.J., Haimberger, L., Healy, S.B., Hersbach, H., Holm, E.V., Isaksen, L., Kallberg, P., Koehler, M., Matricardi, M., McNally, A.P., Monge-Sanz, B.M., Morcrette, J.J., Park, B.K., Peubey, C., de Rosnay, P., Tavolato, C., Thepaut, J.N. and Vitart, F. (2011) The ERA-Interim reanalysis: configuration and performance of the data assimilation system. *Quarterly Journal of the Royal Meteorological Society*, 137(656), 553–597. https://doi.org/10.1002/qj.828

Dohan, K. and Maximenko, N. (2010) Monitoring ocean currents with satellite sensors. *Oceanography*, 23(4), 94–103. https://doi.org/10.5670/oceanog.2010.08

Farchi, A. and Bocquet, M. (2018) Review article: comparison of local particle filters and new implementations. *Nonlinear Processes in Geophysics*, 25, 765–807. https://doi.org/10.5194/npg-25-765-2018

Frei, M. and Künsch, H.R. (2013) Bridging the ensemble Kalman and particle filters. *Biometrika*, 100(4), 781–800. https://doi.org/10.1093/biomet/ast020

Good, S.A., Martin, M.J. and Rayner, N.A. (2013) En4: quality controlled ocean temperature and salinity profiles and monthly objective analyses with uncertainty estimates. *Journal of Geophysical Research – Oceans*, 118(12), 6704–6716. https://doi.org/10.1002/2013jc009067

Hoteit, I., Hoar, T., Gopalakrishnan, G., Collins, N., Anderson, J., Cornuelle, B., Koehl, A. and Heimbach, P. (2013) A MITGCM/-DART ensemble analysis and prediction system with application to the Gulf of Mexico. *Dynamics of Atmospheres and Oceans*, 63, 1–23. https://doi.org/10.1016/j.dynatmoce.2013.03.002

Hunt, B.R., Kostelich, E.J. and Szunyogh, I. (2015) Efficient data assimilation for spatiotemporal chaos: a local ensemble transform Kalman filter. *Physica D Nonlinear Phenomena*, 230(1), 112–126. https://doi.org/10.1016/j.physd.2006.11.008

Kerry, C., Roughan, M. and Powell, B. (2018) Observation impact in a regional reanalysis of the East Australian current system. *Journal of Geophysical Research – Oceans*, 123(10), 7511–7528. https://doi.org/10.1029/2017jc013685

Li, Y. and Toumi, R. (2017) A balanced Kalman filter ocean data assimilation system with application to the south Australian sea. *Ocean Modelling*, 116, 159–172. https://doi.org/10.1016/j.ocemod.2017.06.007

Lorenz, E.N. (2006). Predictability: A problem partly solved. In:, *Predictability of Weather and Climate*. Cambridge, MA: Cambridge University Press.

Metzger, E.J., Smedstad, O.M., Thoppil, P.G., Hurlburt, H.E., Cummings, J.A., Wallcraft, A.J., Zamudio, L., Franklin, D.S., Posey, P.G., Phelps, M.W., Hogan, P.J., Bub, F.L. and DeHaan, C.J. (2014) US Navy operational global ocean and Arctic ice prediction systems. *Oceanography*, 27(3), 32–43. https://doi.org/10.5670/oceanog.2014.66

Morzfeld, M., Hodyss, D. and Poterjoy, J. (2018) Variational particle smoothers and their localization. *Quarterly Journal of the Royal Meteorological Society*, 144(712), 806–825. https://doi.org/10.1002/qj.3256

Mu, Z., Zhang, W., Wang, P., Wang, H. and Yang, X. (2019) Assimilation of SMOS sea surface salinity in the regional ocean model for South China Sea. *Remote Sensing*, 11(8), 919. https://doi.org/10.3390/rs11080919

Nencioli, F., Dong, C., Dickey, T., Washburn, L. and McWilliams, J.C. (2010) A vector geometry-based eddy detection algorithm and its application to a high-resolution numerical model product and high-frequency radar surface velocities in the Southern California bight. *Journal of Atmospheric and Oceanic Technology*, 27(3), 564–579. https://doi.org/10.1175/2009jtecho725.1

Papadakis, N. (2007). Assimilation de donnees images: Applicationau suivi de courbes et de champs de vecteurs. PHD Thesis. Universit´e Rennes 1. Français.

Papadakis, N., Mémin, E., Cuzol, A. and Gengembre, N. (2010) Data assimilation with the weighted ensemble Kalman filter. *Tellus A: Dynamic Meteorology and Oceanography*, 62(5), 673–697. https://doi.org/10.1111/j.1600-0870.2010.00461.x

Penny, S.G. and Miyoshi, T. (2016) A local particle filter for high dimensional geophysical systems. *Nonlinear Processes in Geophysics*, 2(6), 1631–1658. https://doi.org/10.5194/npg-23-391-2016

Pham, D.T. (2001) Stochastic methods for sequential data assimilation in strongly nonlinear systems. *Monthly Weather Review*,

129(5), 1194–1207. https://doi.org/10.1175/1520-0493(2001)129<1194:SMFSDA>2.0.CO;2

Poterjoy, J. (2016) A localized particle filter for high-dimensional nonlinear systems. *Monthly Weather Review*, 144(1), 59–76. https://doi.org/10.1175/MWR-D-15-0163.1

Poterjoy, J. and Anderson, J.L. (2016) Efficient assimilation of simulated observations in a high-dimensional geophysical system using a localized particle filter. *Monthly Weather Review*, 144(5), 2007–2020. https://doi.org/10.1175/mwr-d-15-0322.1

Poterjoy, J., Sobash, R. and Anderson, J.L. (2017) Convective-scale data assimilation for the weather research and forecasting model using the local particle filter. *Monthly Weather Review*, 145(5), 1897–1918. https://doi.org/10.1175/MWR-D-16-0298.1

Poterjoy, J., Wicker, L. and Buehner, M. (2019) Progress toward the application of a localized particle filter for numerical weather prediction. *Monthly Weather Review*, 147(4), 1107–1126. https://doi.org/10.1175/mwr-d-17-0344.1

Potthast, R., Walter, A. and Rhodin, A. (2019) A localised adaptive particle filter within an operational NWP framework. *Monthly Weather Review*, 147(1), 345–362. https://doi.org/10.1175/MWR-D-18-0028.1

Reich, S. (2013) A nonparametric ensemble transform method for Bayesian inference. *Siam Journal on Scientific Computing*, 35(4), A2013–A2024. https://doi.org/10.1137/130907367

Robert, S., Leuenberger, D. and Künsch, H.R. (2017) A local ensemble transform Kalman particle filter for convective scale data assimilation. *Quarterly Journal of the Royal Meteorological Society*, 144(713), 1279–1296. https://doi.org/10.1002/qj.3116

Shchepetkin, A.F. and McWilliams, J.C. (2005) The regional oceanic modeling system (ROMS): a split-explicit, free-surface, topography-following-coordinate oceanic model. *Ocean Modelling*, 9(4), 347–404. https://doi.org/10.1016/j.ocemod.2004.08.002

Shchepetkin, A.F. and McWilliams, J.C. (2009) Ocean forecasting in terrain-following coordinates: formulation and skill assessment of the regional ocean modeling system (vol 227, pg 3595, 2008). *Journal of Computational Physics*, 228(24), 8985–9000. https://doi.org/10.1016/j.jcp.2009.09.002

Tippett, M.K., Anderson, J.L., Bishop, C.H., Hamill, T.M. and Whitaker, J.S. (2003) Ensemble square root filters. *Monthly Weather Review*, 131(7), 1485. https://doi.org/10.1175/1520-0493(2003)131<1485:esrf>2.0.co;2

Todling, R. (2015a) A lag-1 smoother approach to system-error estimation: sequential method. *Quarterly Journal of the Royal Meteorological Society*, 141(690), 1502–1513. https://doi.org/10.1002/qj.2460

Todling, R. (2015b) A complementary note to "A lag-1 smoother approach to system-error estimation": the intrinsic limitations of residual diagnostics. *Quarterly Journal of the Royal Meteorological Society*, 141(692), 2917–2922. https://doi.org/10.1002/qj.2546

Toedter, J., Kirchgessner, P., Nerger, L. and Ahrens, B. (2016) Assessment of a nonlinear ensemble transform filter for high-dimensional data assimilation. *Monthly Weather Review*, 144(1), 409–427. https://doi.org/10.1175/mwr-d-15-0073.1

van Leeuwen, P.J., Kunsch, H.R., Nerger, L., Potthast, R. and Reich, S. (2019) Particle filters for high-dimensional geoscience applications: a review. *Quarterly Journal of the Royal Meteorological Society*, 145(723), 2335–2365. https://doi.org/10.1002/qj.3551

Zhu, M., Van Leeuwen, P.J. and Amezcua, J. (2016) Implicit equal-weights particle filter. *Quarterly Journal of the Royal Meteorological Society*, 142(698), 1904–1919. https://doi.org/10.1002/qj.2784

Zhu, M., van Leeuwen, P.J. and Zhang, W. (2018) Estimating model-error covariances using particle filters. *Quarterly Journal of the Royal Meteorological Society*, 144(713), 1310–1320. https://doi.org/10.1002/qj.3132

APPENDIX A: LWENKF ALGORITHM

This Appendix provides a description of the revised LWEnKF. Symbols used here are listed in Table A1.

1. Forecast each particle up to the analysis time step n to get the prior particles $\mathbf{x}_i^{n,\mathrm{f}} = \mathrm{M}(\mathbf{x}_i^{n-1})$.
2. Use the local perturbed EnKF as the proposal density to obtain the proposal particles $\mathbf{x}_i^0$, $i=1,2,\ldots,N$.
3. For each $k=1,2,\ldots,N_x$, calculate the proposal weight $w_{i,k}^*$ using $\mathbf{x}_i^0$ for $\mathbf{x}_i^n$ in Equations 1-3, and 4. The $\mu_{i,B}^n$ and $\Sigma_{B,D}$ in Equation 2 are computed as follows:

$$\Sigma_{B,D} = (\mathbf{I} - \mathbf{K}_{B,D}\mathbf{H}_B)\mathbf{Q}_B(\mathbf{I} - \mathbf{K}_{B,D}\mathbf{H}_B)^{\mathrm{T}} + \mathbf{K}_{B,D}\mathbf{R}_D\mathbf{K}_{B,D}^{\mathrm{T}}, \quad (A1)$$

$$\mu_{i,B}^n = \mathbf{x}_{i,B}^{n,\mathrm{f}} + \mathbf{K}_{B,D}\left[\mathbf{y}_D - h(\mathbf{x}_i^{n,\mathrm{f}})_D\right], \quad (A2)$$

where the reduced Kalman gain $\mathbf{K}_{B,D}$ is calculated from the prior ensemble:

$$\mathbf{K}_{B,D} = (\mathbf{P}h^{\mathrm{T}})_{B,D}\left[(h\mathbf{P}h^{\mathrm{T}})_D + R_D\right]^{-1}, \quad (A3)$$

$$(\mathbf{P}h^{\mathrm{T}})_{B,D} = \frac{1}{N-1} \times \sum_{i=1}^{N}\left[\mathbf{x}_{i,B}^{n,\mathrm{f}} - \overline{\mathbf{x}_{i,B}^{n,\mathrm{f}}}\right]\left\{[h(\mathbf{x}_i^{n,\mathrm{f}})]_D - \overline{[h(\mathbf{x}_i^{n,\mathrm{f}})]_D}\right\}^{\mathrm{T}}, \quad (A4)$$

$$(h\mathbf{P}h^{\mathrm{T}})_D = \frac{1}{N-1}\sum_{i=1}^{N}\left\{[h(\mathbf{x}_i^{n,\mathrm{f}})]_D - \overline{[h(\mathbf{x}_i^{n,\mathrm{f}})]_D}\right\} \times \left\{[h(\mathbf{x}_i^{n,\mathrm{f}})]_D - \overline{[h(\mathbf{x}_i^{n,\mathrm{f}})]_D}\right\}^{\mathrm{T}}. \quad (A5)$$

4. Calculate the inflation coefficients of the observation error for $j=1,2,\ldots,N_y$.

TABLE A1 List of symbols

Symbol	Description
N_x	Dimension of model variables
N_y	Dimension of observations
N	Number of particles
$\mathbf{x}$	Model variables
$\mathbf{y}$	Observations
μ	Mean of the proposal density
Σ	Covariance matrix of the proposal density
$\mathbf{K}$	Kalman gain matrix
$\mathbf{H}$	Tangent linear observation operator
$h(\cdot)$	Observation operator
$\mathrm{M}(\cdot)$	Forecast model
$\mathbf{Q}$	Model-error covariance matrix
$\mathbf{R}$	Observation-error covariance matrix
B	Local block
D	Local domain
c^B	Half-radius of local block
c^D	Half-radius of local domain
c	Cutoff coefficient for localization function
N_{eff}	Target effective sample size
α	Adjustment parameter for proposal weights
β	Parameter for β inflation
$w_{i,k}^*$	Proposal weight for particle i and model variable k
$w_i^{o,j}$	Likelihood weight calculated from $p(y_j|\mathbf{x}_i^{j-1})$ for particle i and observation j
$l_{j,k}^c$	Localization function value for model variable k when assimilating observation j
$w_{i,k}^j$	Total weight for particle i and model variable k when assimilating observation j
$\tilde{w}_i^j$	Likelihood weight calculated from $p(y_j|\mathbf{x}_i^0)$ for particle i when assimilating observation j
$\mathbf{x}^0$	Proposal particles
$\omega_{i,k}^j$	Localized likelihood weights for particle i and model variable k when assimilating observation j
$\upsilon_{i,k}^j$	Localized total weights for particle i and model variable k when assimilating observation j
Ω_k^j	Normalization factor of localized total weights
$x_{i,k}^j$	Model variable k of particle i when observation j is assimilated
$\bar{x}_k^j$	Weighted mean of model variable k when observation j is assimilated
σ_k^j	Weighted standard deviation of model variable k when observation j is assimilated
$r_{1,k}$	Merging coefficient of model variable k for the total weight
$r_{2,k}$	Merging coefficient of model variable k for the total weight at previous step
γ	Mixing parameter for merging coefficients
$P^{\mathrm{in}}(\cdot)$	Input CDF for the KDDM
$P^{\mathrm{out}}(\cdot)$	Output CDF for the KDDM
$\mathrm{erf}(\cdot)$	Error function
$x_{i,k}^a$	Analysis model variable k of particle i

a. Find $\hat{\beta}_i$ so that the likelihood weights meet the target effective sample size:

$$\hat{\beta}_j = \operatorname{argmin}_\beta \left[N_{\text{eff}} - \frac{\left(\sum\limits_{i=1}^{N} \exp\left\{ \frac{-[y_j - h(\mathbf{x}_i^0)]^2}{2\beta\sigma_{y_j}^2} \right\} \right)^2}{\sum\limits_{i=1}^{N} \exp\left\{ \frac{-[y_j - h(\mathbf{x}_i^0)]^2}{\beta\sigma_{y_j}^2} \right\}} \right] \quad (A6)$$

b. Obtain the multivariate inflation coefficients:

$$\beta_j = 1 + \sum_{m=1}^{N_y} (\hat{\beta}_m - 1) l_{j,m}. \quad (A7)$$

5. Let the initial total weight for each model variable be $w_{i,k}^0 = w_{i,k}^*$. Then, for each $j=1,2,\ldots,N_y$, assimilate the scaler observations y_j one by one.

a. Calculate the likelihood weight for $i=1,2,\ldots,N$ and normalize it:

$$w_i^{o,j} = \frac{\exp\left\{ \frac{-[y_j - h(x_i^{j-1})]}{2\beta_j\sigma_{y_j}^2} \right\}}{\sum\limits_{i=1}^{N} \exp\left\{ \frac{-[y_j - h(x_i^{j-1})]}{2\beta_j\sigma_{y_j}^2} \right\}}. \quad (A8)$$

b. Calculate the total weight for $k\in\{k|l_{j,k}>0\}$:

$$w_{i,k}^j = w_i^{o,j} * w_{i,k}^{j-1}. \quad (A9)$$

c. Update the localized likelihood weight, then derive the localized total weight with its normalization factor for $k\in\{k|l_{j,k}>0\}$ and $i\in\{1,2,\ldots,N\}$:

$$\tilde{w}_i^j = \frac{\exp\left\{ \frac{-[y_j - h(x_i^0)]}{2\beta_j\sigma_{y_j}^2} \right\}}{\sum\limits_{i=1}^{N} \exp\left\{ \frac{-[y_j - h(x_i^0)]}{2\beta_j\sigma_{y_j}^2} \right\}}, \quad (A10)$$

$$\omega_{i,k}^j = \prod_1^j \left\{ \frac{(N\tilde{w}_i^j - 1) l_{j,k}^c + 1}{N} \right\}, \quad (A11)$$

$$\upsilon_{i,k}^j = \omega_{i,k}^j * w_{i,k}^*, \quad (A12)$$

$$\Omega_k^j = \sum_{i=1}^{N} \upsilon_{i,k}^j. \quad (A13)$$

d. Merge the particles for each k in $\{k|l_{j,k}>0\}$ and each i in $\{1,2,\ldots,N\}$:

$$x_{i,k}^j = \bar{x}_k^j + r_{1,k}\left[x_{k,s_i}^{j-1} - \bar{x}_k^j \right] + r_{2,k}\left[x_{k,t_i}^{j-1} - \bar{x}_k^j \right], \quad (A14)$$

$$\bar{x}_k^j = \sum_{i=1}^{N} \frac{\upsilon_{i,k}^j}{\Omega_k^j} x_{i,k}^0, \quad (A15)$$

$$(\sigma_k^j)^2 = \sum_{i=1}^{N} \frac{\upsilon_{i,k}^j}{\Omega_k^j} [x_{i,k}^0 - \bar{x}_k^j]^2, \quad (A16)$$

$$r_{1,k} = \gamma$$

$$\times \sqrt{ \frac{(\sigma_k^j)^2}{\frac{1}{N-1} \sum\limits_{i=1}^{N} \left\{ x_{k,s_i}^{j-1} - \bar{x}_k^j + d_k[x_{k,t_i}^{j-1} - \bar{x}_k^j] \right\}^2} }, \quad (A17)$$

$$r_{2,k} = \gamma(d_k r_{1,k} - 1) + 1, \quad (A18)$$

$$d_k = \frac{N(1 - l_{j,k}^c)}{\tilde{\Omega}_k^j l_{j,k}^c}, \quad (A19)$$

$$\tilde{\Omega}_k^j = \sum_{i=1}^{N} \tilde{w}_i^j \upsilon_{i,k}^{j-1}, \quad (A20)$$

where s_i is the resampled indicator for the current total weight $w_{i,k}^j$ and t_i is the resampled indicator for the total weight at the last step $w_{i,k}^{j-1}$.

e. Update the total weight $w_{i,k}^j = 1/N$ for $k\in\{k|l_{j,k}>0\}$ and $i\in\{1,2,\ldots,N\}$.

6. Adjust the model variables by the KDDM for $k=1,2,\ldots,N_x$.

a. Approximate the input and output cumulative distribution functions (CDFs), respectively:

$$P^{\text{in}}(x_k) = \frac{1}{2} \sum_{i=1}^{N} \left[1 + \operatorname{erf}(\frac{x_k - x_{i,k}^{N_y}}{\sqrt{2}\sigma_k^{N_y}}) \right], \quad (A21)$$

$$P^{\text{out}}(x_k) = \frac{1}{2} \sum_{i=1}^{N} \frac{\upsilon_{i,k}^{N_y}}{\Omega_k} \left[1 + \operatorname{erf}(\frac{x_k - x_{i,k}^0}{\sqrt{2}\sigma_k^0}) \right]. \quad (A22)$$

b. Find the adjustment for $i=1,2,\ldots,N$ using the cubic spline interpolation, and obtain the analysis particles:

$$p_{i,k} = P^{\text{in}}(x_{i,k}^{N_y}), \quad (A23)$$

$$x_{i,k}^a = (P^{\text{out}})^{-1}(p_{i,k}). \quad (A24)$$